Acta Materialia 178 (2019) 135–145

Contents lists available at ScienceDirect

Acta Materialia

journal homepage: www.elsevier.com/locate/actamat

Full length article

# Density, distribution and nature of planar faults in silver antimony telluride for thermoelectric applications

Lamya Abdellaoui [a], Siyuan Zhang [a], Stefan Zaefferer [a, **], Ruben Bueno-Villoro [a], Andrei Baranovskiy [b], Oana Cojocaru-Mirédin [c], Yuan Yu [c], Yaron Amouyal [b], Dierk Raabe [a], Gerald Jeffrey Snyder [d], Christina Scheu [a, *]

[a] Max-Planck Institut für Eisenforschung GmbH, Max-Planck Straße 1, 40237, Düsseldorf, Germany
[b] Department of Materials Science and Engineering, Technion–Israel Institute of Technology, Technion City, 32000, Haifa, Israel
[c] Institute of Physics, RWTH Aachen University, Sommerfeldstraße 14, 52056, Aachen, Germany
[d] Northwestern University, Materials Science and Engineering Department, 2220 Campus Drive, Evanston, IL, 60208-3109, USA

ARTICLE INFO

*Article history:*
Received 28 May 2019
Received in revised form
18 July 2019
Accepted 19 July 2019
Available online 23 July 2019

*Keywords:*
Thermoelectric materials
Silver-antimony-telluride compounds
Thermal conductivity
Electron microscopy
Planar faults

ABSTRACT

Defects such as planar faults in thermoelectric materials improve their performance by scattering phonons with short and medium mean free paths (3–100 nm), thereby reducing the lattice thermal conductivity, $\kappa_l$. Understanding statistically the microscopic distribution of these extended defects within the grains and in low angle grain boundaries is necessary to tailor and develop materials with optimal thermoelectric performance for waste heat harvesting. Herein, we analyze these defects from the millimeter down to the nanometer scale in a $AgSbTe_2$ thermoelectric material with low angle grain boundaries. The investigations were performed using electron channeling contrast imaging combined with transmission electron microscopy. The microstructure study was complemented by estimating the effect of planar faults on the phonon scattering using the Debye-Callaway model. $AgSbTe_2$ is a promising thermoelectric material, which exhibits extremely low thermal conductivity, $\kappa$, of 0.5 $Wm^{-1}K^{-1}$ at room temperature. In contrast to conventional alloys or intermetallic materials, in the present material small angle grain boundaries are not composed of individual dislocations but of a dense arrangement of stacked planar faults with fault densities up to $N_{PF} = 1.6 \cdot 10^8\ m^{-1}$. We explain their abundance based on their low interfacial energy of about 186 $mJm^{-2}$ calculated *ab-initio*. The current findings show, that it is possible to reach very high densities of phonon-scattering planar faults by the correct microstructure engineering in $AgSbTe_2$ thermoelectric materials.


## 1. Introduction

Interest in thermoelectric (TE) materials is growing due to their potential in converting waste heat from e.g. automotive exhausters, power plants, thermal sensors, etc., into electricity [1–8] and thus reducing dependence on fossil fuels [9]. The conversion efficiency of TE materials is related to the figure of merit, $zT$, which is determined by the material properties: $zT = \alpha^2 \sigma T / \kappa$. Here $\alpha$ is the Seebeck coefficient, $\kappa$ is the thermal conductivity, $\sigma$ is the electrical conductivity, and $T$ is the absolute temperature. The thermal conductivity is the sum of two components: $\kappa_e$ due to electrons and holes conducting heat and $\kappa_l$ associated to phonons propagating through the lattice [10], $\kappa_{tot} = \kappa_e + \kappa_l$. A high $zT$ factor requires low $\kappa$ and high $\alpha$ and $\sigma$-values.

The ternary complex chalcogenide $AgSbTe_2$ is one of the most promising p-type semiconducting compounds for mid-range temperature (400–700 K) TE power generation [7,10–14]. The material is solidified as stable single $\delta$-phase enriched with Sb and Te, which is compositionally located beyond the stoichiometric $AgSbTe_2$ composition and extends from 29 to 31 at. % Sb at 556 °C as described in the pseudo-binary phase diagram [15]. The $Ag_{16.7}Sb_{30}Te_{53.3}$ -$\delta$-phase has a rock-salt NaCl-type structure where Te atoms occupy the Cl sites and Ag, Sb atoms randomly occupy the Na sites [16], with deviations from the cubic symmetry under special conditions [14]. The lattice constant is a = 0.5786 nm at

* Corresponding author.
** Corresponding author.
*E-mail addresses:* s.zaefferer@mpie.de (S. Zaefferer), c.scheu@mpie.de (C. Scheu).

https://doi.org/10.1016/j.actamat.2019.07.031

room temperature. The δ-phase is metastable and decomposes below 635 K into two stable phases in a eutectoid transformation [17] according to $\delta \rightarrow Sb_2Te_3 + Ag_2Te$.

Promising TE materials have small κ- values. In particular, it is important to reduce their lattice contribution to κ as much as possible by introducing various phonon scattering centers in the matrix. The $AgSbTe_2$-δ-phase has an intrinsically low lattice thermal conductivity in the order of $\kappa_l = 0.68\ Wm^{-1}K^{-1}$ at 400 K, due to its glass like phonon scattering [12,18,19], and its unconventional chemical mechanism as shown recently by Min Zhu et al. [20]. The highest *zT* factor that has been measured for the pristine $AgSbTe_2$ bulk materials was 1.3 at 720 K [12,21,22], Solid solutions of $AgSbTe_2$ with GeTe and PbTe alloys, such as the quaternary compounds Pb-Ag-Sb-Te [8,23]and $(AgSbTe_2)_{1-x}(GeTe)_x$ [24–26], exhibit higher TE performance e.g. zT = 1.7 at 700 K for $(AgSbTe_2)_{9.09}(PbTe)_{90.91}$ reported in Hsu et al. [27].

Several approaches were applied to reduce $\kappa_l$ in $AgSbTe_2$- based compounds. For example, doping with solute elements to introduce point defect phonon scattering which leads to a value of $\kappa_l = 0.4\ Wm^{-1}K^{-1}$ at 400 K and a *zT* ~ 1.9 at 585 K in p-type $AgSb_{0.96}Zn_{0.04}Te_2$ a in the work of Roychowdhury et al. [28]. Formation of second phases via solid-state precipitation is used to initiate phonon scattering at the resulting interfaces. For example, $Sb_2Te_3$ precipitates with sizes ranging from nanometer to micrometer led to a $\kappa_l = 0.65\ Wm^{-1}K^{-1}$ at 300 K [29,30] in $Ag_{16.7}Sb_{30}Te_{53.3}$ alloys. Introducing a high density of grain boundaries, i.e. reducing the grain size, enables also effective phonon scattering as proposed by Dresselhaus et al. [31]. In particular grain boundaries containing dislocations [32], i. e. low-angle grain boundaries (LAGBs), and dislocations within grains can significantly reduce $\kappa_l$ as demonstrated by Chen et al. [33]. They reported on $\kappa_l = 0.4\ Wm^{-1}K^{-1}$ resulting in a *zT* = 2.2 at 850 K in $Na_{0.025}Eu_{0.03}Pb_{0.945}Te$ TE alloys. Interfacial dislocations found in $PbTe_{0.7}S_{0.3}$ lead to $= 0.8\ Wm^{-1}K^{-1}$ at room temperature [34,35].

Formation of planar faults in $AgSbTe_2$ alloys was discussed in several studies [29,36,37]. In 2010, Sharma et al. [36] investigated planar faults in an as-quenched $Ag_{16.7}Sb_{30}Te_{53.3}$-δ-phase. They found that most planar defects were stacking faults (SFs) forming a percolating network. The SFs were observed at the micro- to nanometer scale using transmission electron microscopy (TEM), and found to lie on the {111} planes. Hong et al. showed that high density of SFs ($8 \times 10^6\ m^{-1}$) in $AgSbTe_2$, has a large and positive effect on phonon scattering leading to $\kappa_l = 0.32\ Wm^{-1}K^{-1}$, and an improved *zT* up to 2 at T = 600 K for p-type $AgSbTe_{1.85}Se_{0.15}$ alloys [38].

In an earlier study, we investigated $Ag_{16.7}Sb_{30}Te_{53.3}$, in the as-quenched δ-phase state with zT~ 0.5 at 600 K [39]. In the present work, we analyze the same as-quenched δ-phase in form of a single crystal with a mosaic structure. Such mosaic structures consist of sub-grains with nearly identical orientations and boundaries of only small misorientation angles [17,40–43]. The large lattice coherency in a mosaic crystal of $Cu_2Se_{0.5}Te_{0.5}$ bulk TE material resulted in an excellent σ, while the LAGBs with 10–20 nm size grains were still very efficient in scattering the heat conducting phonons resulting in a $\kappa_l = 0.8\ Wm^{-1}K^{-1}$ at 650 K and $\kappa_l = 0.5\ Wm^{-1}K^{-1}$ at 1000 K [44]. Similarly, due to the complex structural characteristics, the mosaic δ-phase of $Ag_{16.7}Sb_{30}Te_{53.3}$ possesses a low lattice thermal conductivity ($\kappa_l$~0.6 $Wm^{-1}K^{-1}$) at T = 300 °C [39].

Despite the common practice of defects engineering in $AgSbTe_2$ alloys, fundamental understanding of the crystallography and spatial distribution of defects is still limited. In this article, we extend this knowledge by analyzing the distribution of defects from the millimeter down to the nanometer length scales. To achieve this, we combine various scanning electron microscopy (SEM) techniques, in particular electron backscatter diffraction (EBSD) and electron channeling contrast imaging (ECCI) [45]. The density of the planar faults is evaluated over multiple grains with several hundreds of micrometer size. Transmission and scanning transmission electron microscopy (TEM/STEM) are used to analyze the defects and their distribution in the vicinity of LAGBs. In addition, the effect of such defects on $\kappa_l$ is discussed based on the Debye-Callaway model, [46] which enables the evaluation of the necessary number density of planar faults to reduce $\kappa_l$. The density functional theory (DFT) calculations have been performed to explain the formation of the planar faults.

In this work, we address three basic questions: (1) how does the solidification process of $Ag_{16.7}Sb_{30}Te_{53.3}$-δ phase materials affect the microstructure evolution and lead to a mosaic microstructure with planar faults located at the LAGBs? (2) What is the number density of planar faults and how does this density change at the LAGBs toward the interior of the grains? (3) How does the high density of planar faults influence the lattice thermal conductivity?

Answering these questions will help us understanding the microstructure design principles of mosaic TE crystals and estimate their effects on TE transport coefficients.

## 2. Experimental and computational procedures

### 2.1. Sample synthesis

The alloy used in this study has the nominal composition $Ag_{16.7}Sb_{30}Te_{53.3}$ (at. %). It was prepared by primary melting of high-purity elements (4–5 N) at 850 °C for 2.5 h in 12.7 mm diameter quartz ampoules refilled with a ca. 100 torr Ar- 7 vol % $H_2$ mixture, followed by a vacancy annihilation heat treatment at 600 °C for 2 h [39]. Formation of the single δ-phase is obtained by slow cooling (−5 °C/h) down to 556 °C. Due to the slow cooling from top to bottom a well-defined preferred solidification direction is obtained in the sample. Homogenization heat treatment has been performed for 80 h at 556 °C. This process was terminated by quenching the material in ice-water. Further details are reported elsewhere [39].

### 2.2. Structural analysis

Microstructural characterization was carried out using SEM. The microstructure of the δ-phase single-crystal was revealed by EBSD mapping using a large step size of 10 μm in order to cover a 25 $mm^2$ area of the sample. EBSD mapping was performed using a JEOL JSM-6500F FEG-SEM equipped with an EDAX/TSL EBSD system with a Digiview IV camera. The measurements were carried out at an accelerating voltage of 15 kV, a beam current of 15 nA and a working distance of 18 mm. Analysis of the spatial distribution of planar faults at the microscale was performed using ECCI [45]. The samples were prepared for these measurements by grinding with SiC paper followed by OPS + $H_2O_2$ polishing. Finally, in order to remove fine scratches, the surface was polished using a grazing incidence Argon ion beam in a GATAN Model 682 PECS with a voltage ranging from 2 to 3 kV, rotation of 10 rpm, and an inclination angle of 85°. The ECCI experiments were done at an accelerating voltage of 30 kV, a beam current of 2 nA, and a working distance of 7–7.5 mm, using a Zeiss MERLIN SEM microscope. The density and character of planar faults was determined by ECCI under controlled diffraction conditions. For this, the crystal orientation was first measured using a Bruker EBSD system with a BRUKER $e^-$ FLASH camera in the Zeiss MERLIN SEM. From these data the sample tilt and rotation angles required to obtain two-beam diffraction conditions were calculated using the computer program TOCA [45] and the sample was analyzed using the obtained values.

Further microstructural analysis was carried out using TEM. A site-specific TEM lamella was prepared using the focused ion beam (FIB) technique with dual-beam instruments (FEI Helios NanoLab 600 and 600i TM). A cleaning cross section mode was used to thin the lamella to 100 nm, followed by a low-energy (5 keV) Ga beam milling as a final ion-milling step to minimize the beam damage as described in Ref. [47]. Bright and dark field TEM investigations were carried out using a PHILIPS CM20 TEM operated at 200 kV. STEM was performed using a Titan Themis microscope with aberration-corrected probe operated at 300 kV. The aberration corrected probe had a size of ~1 Å and a convergence semi-angle of 24 mrad. For imaging a high angle annular dark field (HAADF) detector with a collection angle range of 73–200 mrad was used.

For quantitative analysis of the defect density using ECCI, 10 micrographs were collected at LAGBs and grain interior with a total analyzed area of around 300 · 300 $\mu m^2$. In TEM, 43 micrographs were collected at the LAGBs and adjacent areas with a covered area of 3 · 3 $\mu m^2$.

### 2.3. Computational procedure

The formation of planar lattice defects is associated with the magnitude of the SFs energy (SFEs) in the material. Therefore, SFEs were evaluated from the total energy values, calculated using density functional theory (DFT) [48–50], and applying the Vienna *Ab initio* Simulation Package (VASP) [51], which uses plane-waves as basis set to expand the total wave function [52]. The electronic exchange-correlation energy was treated within the generalized gradient approximation (GGA) in the framework of revised Perdew–Burke–Ernzerhof (PBE-sol) functionals [53]. The cut-off energy for the plane wave was chosen to be 325 eV. Total energy calculations were performed applying a fine *k*-mesh grid with density <0.2 $Å^{-1}$. All structures were relaxed such that the ionic forces reduced to values below 0.02 eV $Å^{-1}$, with the self-consistent electronic energy for each ionic step converged below $10^{-6}$ eV.

## 3. Results

### 3.1. Overview of the sub-grains in the sample

Using EBSD and ECCI, LAGBs were detected and mapped in the as-quenched sample as displayed in Fig. 1(a). In a cross section perpendicular to the solidification direction, the sub-grains appear to have an irregular shape with an average diameter of about 500 μm. In the present material, the LAGBs are not sharp and have a width of about several μm. This is visible in the orientation gradient of the kernel average misorientation (KAM) map in Fig. 1(b). On the radial direction cross section parallel to the solidification direction, the sub-grains show a strongly elongated shape as revealed in Fig. 1(c&d). It can thus be concluded that in 3D these sub-grains have a columnar shape as sketched in Fig. 1(e). The misorientation angle across the LAGBs is 1–2° as measured by EBSD. All sub-grains are oriented such that a <111> direction is almost parallel to the solidification direction, as indicated by the {111} pole figure displayed in lower part of Fig. 1(e). This means that the surface of the solidification direction cross section is almost parallel to a {111} plane, with a deviation of ~ 8°.

### 3.2. Analysis of the LAGBs

Detailed analysis of the LAGBs was done by ECCI as exemplary shown for one LAGB in Fig. 2. The KAM based micrograph shows that the chosen LAGB reveals a misorientation angle of 1.7° and exhibits a width of 4 μm (Fig. 2(a)). The corresponding ECC image is presented in Fig. 2(b). Here the lower sub-grain has been tilted into two beam conditions for $g = (\bar{4}42)$ and thus appears dark. Thin bright lines inside the grain are visible. The LAGB appears as a bright band, with sharp protrusions into the sub-grains on both sides. A further zoom-in into the LAGB in Fig. 2(c) shows that it displays a dense arrangement of the thin white lines. The brightness of the area indicates a high amount of lattice defects in this area, which degrades the channelling conditions and turns over to intense backscattering. Using the stereographic projection of the crystal orientation (Fig. 2(g)) it is possible to assign plane traces to all defects visible in the lower grain in Fig. 2(c), as marked by green (A), red (B) and purple (C) lines. Finally, Fig. 2(d) shows a magnified ECC image of the region marked by a yellow rectangle in Fig. 2(c) with $g = (011)$ indicated by a yellow arrow. This image shows features that are difficult to interpret and, therefore, need careful analysis. First and foremost, the image shows intense white lines, almost perfectly straight and parallel to the $[\bar{1}21]$ direction. The lines show slight undulations and some of them turn abruptly in a new line which continues under a sharp angle and fades into the depths of the material, as marked by white arrows. Although these features appear like line-defects (i.e. dislocations) they are actually not, for the following reasons: the lines are perfectly parallel to the surface (no contrast change along the line) and the strength of the contrast indicates that they are directly at the surface or very shortly below that. As these features are unlikely to appear for dislocations we suggest an alternative explanation by the fact, that the lines are exactly parallel to the trace of the {111} planes, which are almost exactly parallel to the surface. Thus, it may be assumed that the lines mark the intersections of planar defects on {111} planes with the surface, plotted as light blue lines in the stereographic projection, and referred to as 'D'. As sketched in Fig. 2 (h) from the distance between the lines, H (~10 nm between some lines, 50 … 100 nm between other lines) and the known angle of the {111} planes with the surface, θ, (max. 8°) a spacing between these planar features, d, of about 1.4–14 nm is calculated.

Similar line features as in Fig. 2(d) were observed in all LAGBs regions of the same sample and another corresponding example is displayed in Fig. 3(a), with $g = (\bar{1}10)$ is the channelling condition and their plane trace is plotted in the stereographic projection shown in Fig. 3(c). The assumption that these lines are planar faults is further confirmed when tilting the sample to a different diffraction vector, e.g. $g = (0\bar{1}1)$ as displayed in Fig. 3(b). Here the intense lines have disappeared and, instead, densely overlapping planar defects become visible by high brightness, fading with depth for every line from left to right. Furthermore, as in Fig. 3(a&b), some of the planes are terminated by white lines (indicated by white arrows) which in both images resemble dislocations, as they are curved, sharp and fade with depths below the surface. A number of further *g*-vectors were tested such as $g = (\bar{1}11)$, $g = (\bar{1}\bar{1}1)$, $g = (4\bar{2}\bar{4})$, $g = (10\bar{1})$, all of which resulted in visibility of the planar defects. From these observations, it is concluded that the situation with $g = (011)$ and $g = (\bar{1}10)$ in Figs. 2(d) and 3(a) respectively corresponds to invisibility of the planar defects, although their edges are clearly visible, while all other conditions correspond to visibility although in these cases the edges are significantly less obvious. The reason for the strong visibility of the edges under $g = (\bar{1}10)$ is not yet clear but it is assumed that these lines indicate some sort of surface reconstruction of planar faults intersecting with the free sample surface which leads to strong backscattering in an otherwise strong channelling situation. In this regard, Picard et al. [54] demonstrated that surface reconstruction may lead to strong visibility of dislocations which, according to the $\boldsymbol{g}\cdot\boldsymbol{b}=0$ criterion should be invisible. The same principles may be applied to the planar features in our work.

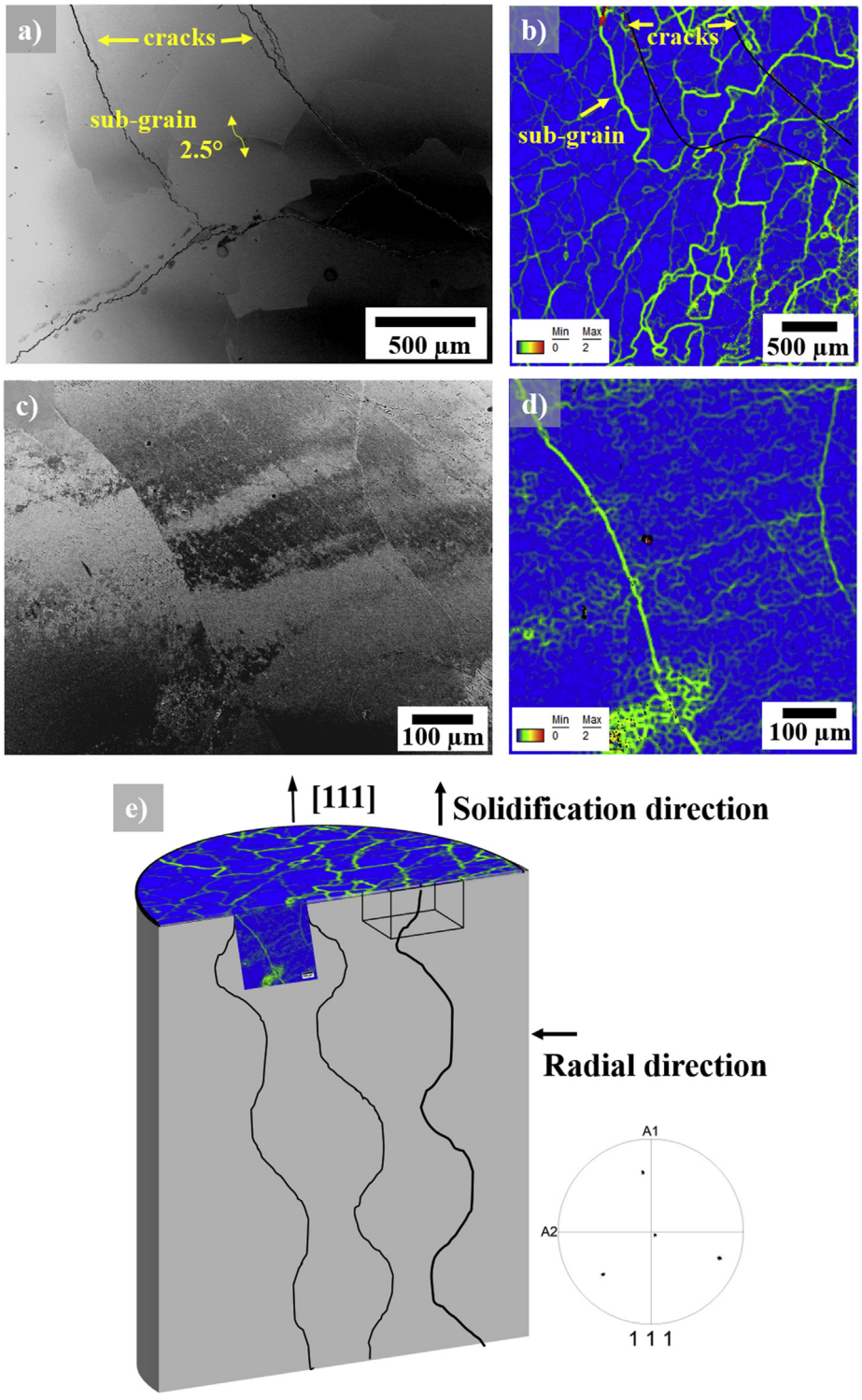


**Fig. 1.** (a) ECC image of a region from the mosaic crystal showing the sub-grains with small angle grain boundaries. (b) Kernel average misorientation map from an EBSD scan of the same area (lower magnification) showing that most misorientation are within 1–2°. (c) ECC image of a cross section from the region in (a). (d) EBSD-Kernel average misorientation map showing elongated grains from a part of the same region shown in (c). (e) sketch visualizing the solidification direction parallel to [111], and the radial direction of the mosaic crystal.

### *3.3. Correlative ECCI-TEM and density investigation of planar faults*

ECCI and TEM observations were carried out with the aim to calculate the density of defects at the LAGBs and in the interior of the grains, in order to compare both of them at a larger scale, using the same LAGB displayed in Fig. 2.

The density of the planar faults at the LAGB and inside the grains is an important measure for the phonon scattering. Planar fault densities are quantified as interface area per volume, termed as 'linear density, $N_{PF}$. The density can be estimated by the total planar

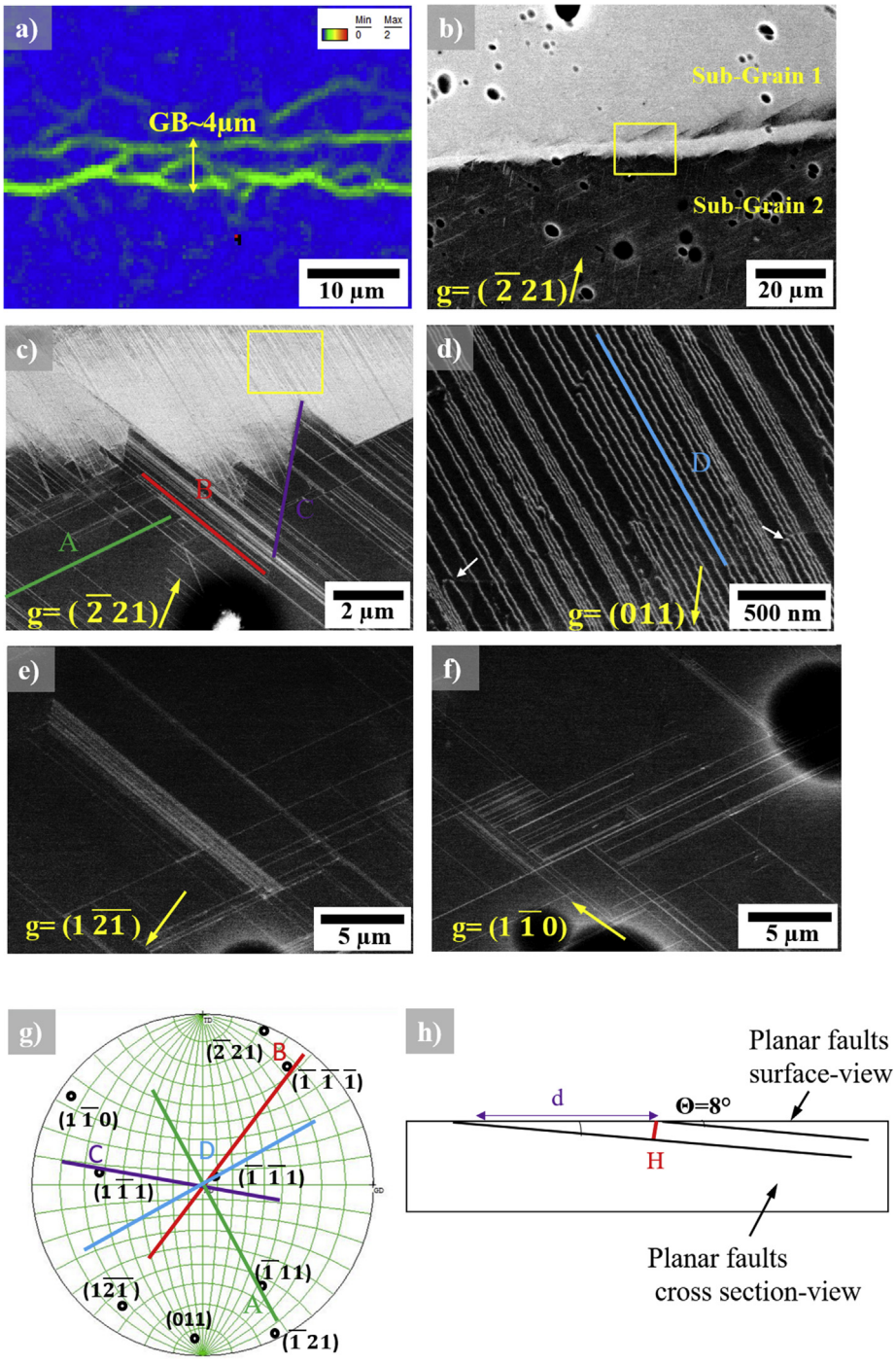


**Fig. 2.** (a) EBSD- Kernel average misorientation map of a low angle grain boundary region with miorientation angle of 1.8° and (b) ECC image with the lower grain from (a) oriented in g = ($\bar{4}42$) channeling condition. (c) Magnified view of the area marked in b) with a yellow box showing the visibility of three set of planar defects A,B, and C at g=($\bar{2}21$) 2-beam condition. (d) Magnified area shown with a yellow box in (c) displaying a fourth set of planar defects referred as D, taken at channeling condition g=(022). (e) ECCI image showing the lower grain 100 µm away from the LAGB. (f) ECCI image showing the upper grain located 100 µm away from the LAGB. (g) Stereographic projection showing that the sets of planar faults A,B, C and D are lying on (11 $\bar{1}$), ($\bar{1}$11) , (1$\bar{1}$1) and ($\bar{1}\bar{1}$1) planes respectively. h) Schematic drawing of the planar defects labelled as set D in d) where *d* is the distance between their intersection with the surface and *H* their spacing. (For interpretation of the references to colour in this figure legend, the reader is referred to the Web version of this article.)

fault area over the observed volume according to,

$$N_{PF} = \frac{\sum l \cdot h}{A_0 \cdot h} \cdot \frac{1}{\sin\theta} = \frac{\sum l}{A_0} \cdot \frac{1}{\sin\theta} \qquad \text{Equation 1}$$

With $l$ being the length, $h$ the depth of the PFs, $A_0$ being the area of measurement, and $\theta$ is the angle between the planar fault and the surface of the sample. This angle needs to be taken in consideration for ECCI density calculation while for the TEM measurements the angle $\theta$ is 90°.

Using the approach above, several values were calculated. The density of planar faults A, B, and C at the LAGB are

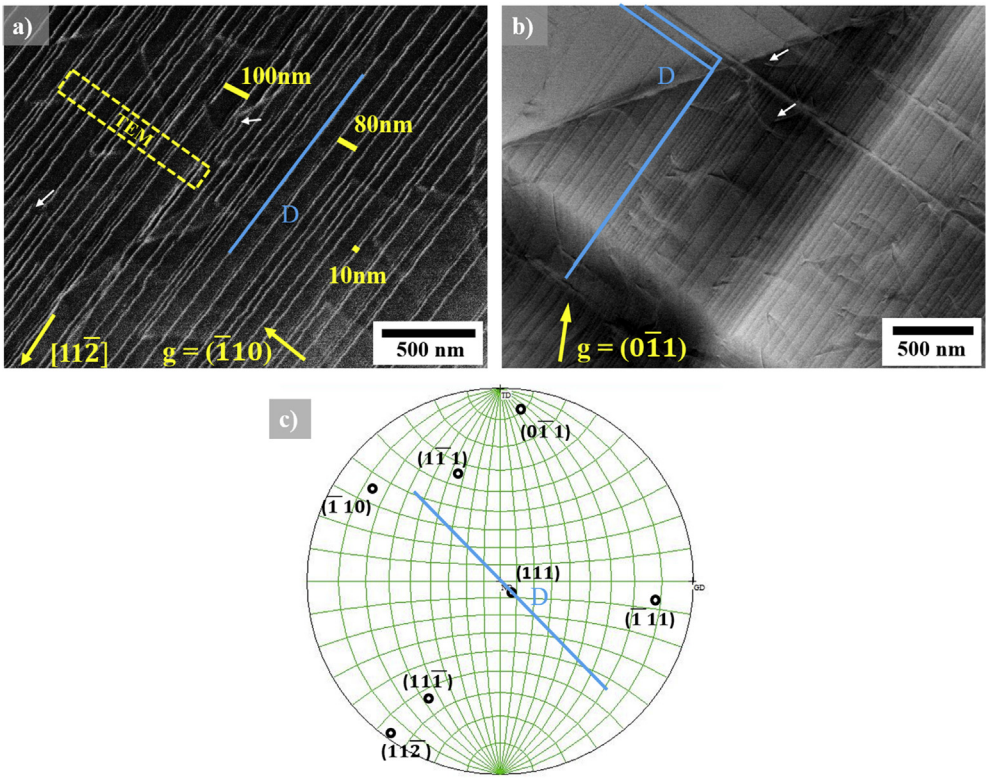


**Fig. 3.** (a) Magnified LAGBs area containing similar features as observed in Fig. 2(d) at g=($\bar{1}$10) 2-beam condition where the planar faults are invisible but their intersection with the surface is visible. (b) Same area shown in (a) at g=(0$\bar{1}$1) 2-beam condition where the planar faults of type D are visible and overlaping. (c) Stereographic projection showing the (111) plane on which this planar faults are lying.

$N_{PF} = 7.5 \cdot 10^5\ m^{-1}$ , $N_{PF} = 5.3 \cdot 10^6\ m^{-1}$ and $N_{PF} = 3.6 \cdot 10^5\ m^{-1}$ , respectively, as determined from Fig. 2(c).

For the planar faults D at the LAGB, which are visible after tilting to channelling condition of $g = (011)$ (Fig. 2(d)), only their intersections with the surface are visible in the ECC image as explained in the previous section. Therefore, the geometrical factor described in equation (1) has to be taken into consideration for calculating their density. A schematic drawing of these defects inclined to the surface with an angle $\theta$ is shown in Fig. 2 (h). The angle $\theta$ is given by $\sin\theta = H/d$. Here, $d$ is the distance between the intersecting defects lines visible at the surface, and $H$ the spacing between the planar faults as shown in the schematic cross section. The spacing of planar faults is related to their density $H = 1/N_{PF}$.

Using $\theta = 8°$ and the measured distance $d$, we evaluate $N_{PF} = 1.6 \cdot 10^8\ m^{-1}$ for planar faults of type D. Two areas representing the interior of the grains are shown in Fig. 2(e&f) which are located 100 μm away from the GB in sub grain 1 and 2 respectively. Here, we calculated values of $N_{PF} = 1.7 \cdot 10^6\ m^{-1}$ *and* $N_{PF} = 1.5 \cdot 10^6\ m^{-1}$. A similar behavior was observed at distances closer and further away from the LAGB, i.e. the density of planar faults decreases two order of magnitude compared to the values at the LAGB.

In order to prove that the boundary described in section 3.2 is composed of inclined planar faults with 8° toward the surface at the LAGB, we used a FIB instrument to lift out a cross section lamella from the area marked with a yellow rectangle in Fig. 3(a) and investigated it by TEM. The crystallographic directions taken from the TEM studies are, thus, perpendicular to that of ECCI. The TEM image of the LAGB region, where one grain is tilted towards the [$\bar{1}$11] zone axis, is shown in Fig. 4(a). The corresponding diffraction pattern is shown as an inset. The bright field image reveals the same set of planar faults that are shown in the ECC images in Figs. 2 and 3. The planar faults intersect the free surface (coated with Pt), forming an inclination angle of ~8° with respect to the solidification direction. They are indicated by the yellow lines and possess a high density of $N_{PF} = 1.5 \cdot 10^8\ m^{-1}$. Inside the grain, which is imaged along the [011] zone axis (Fig. 4(b)), the density was estimated to be much lower and quantified as $N_{PF} = 1.1 \cdot 10^6\ m^{-1}$.

Finally, STEM was applied to determine the distance of the planar faults at the nanometer length scale. The sample was tilted until the planar faults were observed exactly edge-on in the HAADF image, with the zone axis being [211] as shown in the Fast Fourier transform (Fig. 4(c)). A zoomed-in HAADF image is given in Fig. 4(d). The distance between the (111) planes is 0.25 nm. The faults resolve into individual planar features or groups of equally-spaced individual features with a density of $N_{PF} = 1.5 \cdot 10^8\ m^{-1}$ at the LAGB. This density matches the density observed from ECCI. The smaller distances between two faults are about H = 1.4 nm with a variation of 1 or 2 atomic layers. The distance between groups of planar defects is in the order of 10–14 nm. These numbers agree with the spacing calculated in the previous section from the ECCI images.

### 3.4. Evaluating the planar fault energy from first-principles

To account for the high density of planar faults detected experimentally, we calculate their energies, specifically the SFEs, provided that low SFEs yield high SF densities. The low values of SFEs make the calculation challenging, especially when correlation between the SFE and the alloy chemistry is required. We construct two 64-atom supercells having the $AgSbTe_2$ stoichiometry, and introduce a SF applying a [112]-translation on the (111) plane, Fig. 5.

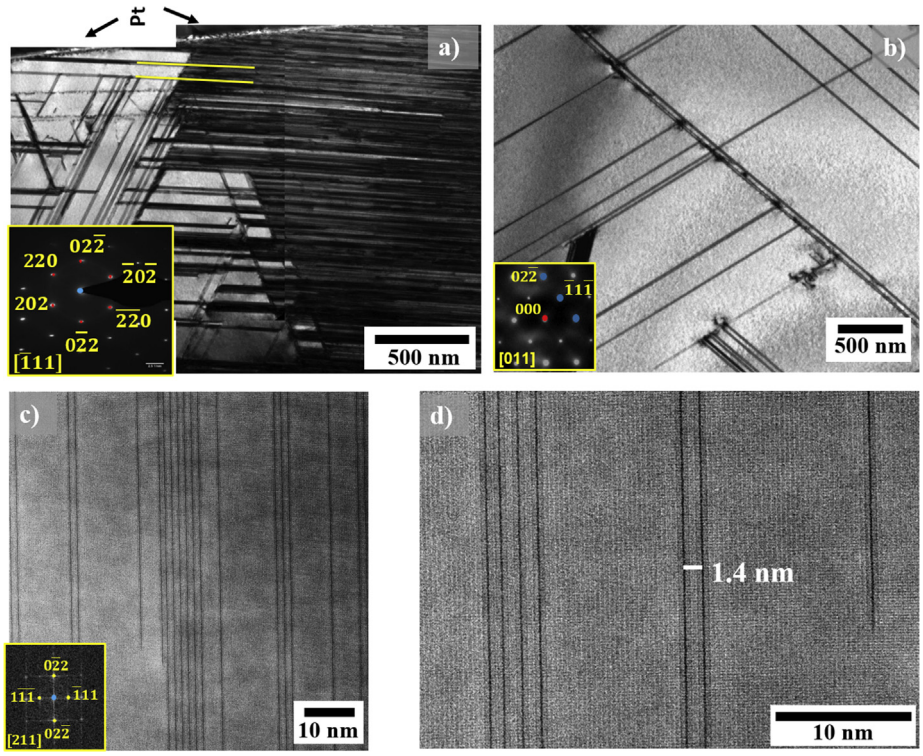


**Fig. 4.** (a) Bright-field TEM image of the FIB lamella taken from the region marked in Fig. 3(a), the corresponding diffraction pattern in [11$\bar{1}$] zone axis is shown as inset in the lower left part. The inclination of the planar faults relative to the surface (covered with a Pt layer) is visible. (b) Bright field image of a FIB lamella taken from inside of another grain showing planar faults with lower density. (c) and (d) HAADF micrographs of individual as well as groups of planar defects.

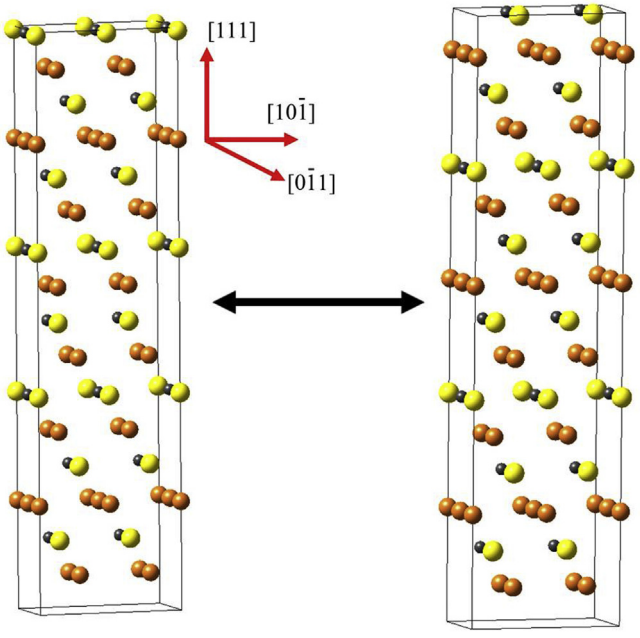


**Fig. 5.** Two simulation cells of 64 atoms each having the $AgSbTe_2$ stoichiometry with (left) and without (right) a 1/6 (111)[112] stacking fault (SF) indicated by the arrow. Black, yellow, and orange spheres represent Ag, Sb, and Te atoms, respectively. (For interpretation of the references to colour in this figure legend, the reader is referred to the Web version of this article.)

The base supercells are constructed using a PbTe cubic supercell containing 32 atoms of Pb and Te having the Fm$\bar{3}$m space group symmetry. Then, 16 randomly selected Pb-atoms are substituted with Ag, and the other 16 with Sb. As a result, we obtain quasi-random assemblies representing the semi-disordered structure of $AgSbTe_2$. The SFE, $\gamma$, is evaluated from the difference of total energies between both cells according to:

$$\gamma = \frac{1}{A^*}(E_{SF} - E), \qquad \text{Equation 2}$$

Where $E_{SF}$ and $E$ are the total energies of the structure with or without a SF, respectively, and $A^*$ is the SF area. We apply periodic boundary conditions on both simulation cells, and make sure that they are adequately large (here: 30 Å) to avoid interaction between two neighbouring SFs.

We performed total energy calculations for both supercells, with or without SFs, having different Ag/Sb permutations, to reflect the variance resulting from occupying the Pb-sublattice sites by these two atoms with different options. We tested six permutations in total, and the resulting supercell total energies per atom are summarized in the plot displayed in Fig. 6. It is shown that the presence of SFs increases the total energies, as expected, and that the difference between both options (with or without SF) depends on the Ag/Sb permutation. Overall, all values of total energy per atom range between the standard chemical potentials of Sb and Te.

The results shown in Fig. 6 enable us to evaluate the SFEs from equation (2), and the minimum value is 185.9 mJ m$^{-2}$, while the average SFE is evaluated to be 260.4 mJ m$^{-2}$. Besided the minimum SFE value, we highlight that it is important to consider the variance of the total energy values as well, since there are many options to occupy 16 Sb-atoms in 32 Pb-sublattice sites (and the rest to be occupied by Ag-atoms), out of which only six permutations were tested. The other permutations that were not tested might have exhibited SFEs <185.9 mJ m$^{-2}$; for this reason, we refer to the value of 185.9 mJ m$^{-2}$ as the upper limit of SFE in this 1/6 (111) [112]

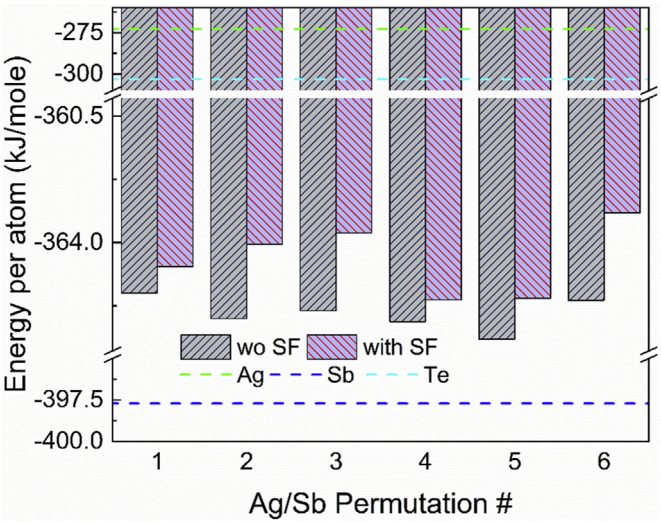


**Fig. 6.** The total energy per atom calculated ab-initio for the supercells having different Ag/Sb permutations without SFs and with SFs, indicated by grey or magenta bars, respectively. For reference, the standard chemical potentials of Ag, Sb, and Te are indicated as horizontal dashed green, blue, and aqua lines. (For interpretation of the references to colour in this figure legend, the reader is referred to the Web version of this article.)

system. Furthermore, the variance of the total energy values, from which SFE-values are derived, is estimated to be ca. 1.1% of the average total energy, Fig. 6, meaning that our calculated SFEs are relatively stable against lattice disordering, which validates the reliability of these calculations.

## 4. Discussion

The microstructure observed by EBSD suggests that the sample was created by directional solidification leading to the formation of grains with small misorientations. The preferred growth direction from the undercooled melt in the studied crystal was [111]. Due to thermal stresses during nucleation, slightly misoriented grains grow parallel to the solidification direction, leading to the columnar subgrains observed in the material. The resulting microstructure is summarized in Fig. 1(e).

The combination of ECCI and TEM conducted in this work provides us with a consistent overview of the distribution of planar faults in the $Ag_{16.7}Sb_{30}Te_{53.3}$-δ phase. We found that the density of planar faults calculated from ECC images is matching the one calculated from TEM. The planar fault density was calculated to be $N_{PF} = 1.6 \cdot 10^8 m^{-1}$ at the LAGBs. This is a much higher density than that found in the interior of the grains, $N_{PF} = 1.5 \cdot 10^6\ m^{-1}$. Controlled ECCI performed at exact Bragg conditions revealed excellent contrast for investigation of planar faults, which was very useful to understand the nature of these faults and accomplish a good picture of their location and directions. A schematic representation of the network of planar defects at the grain boundary is given in Fig. 7(a&b). The small misorientation angle (1.7°) is not compensated by perfect dislocations (Fig. 7(a)) but by extended planar faults (Fig. 7(b)). The sketch of the planar faults structure observed in ECCI and TEM lying on the {111} planes with 8° inclination angle to the surface is presented in Fig. 7(c).

It is noteworthy that previously reported first-principles calculations of interfacial free energies of the $AgSbTe_2/Sb_2Te_3$ and $AgSbTe_2/Sb_8Te_3$ systems yield values as low as 208 and 175 mJ $m^{-2}$, respectively [55], which are similar to those calculated in this study. Such similarity is not surprising, since these $AgSbTe_2/Sb_2Te_3$ and $AgSbTe_2/Sb_8Te_3$ interfaces feature extremely small interfacial atomic misfit and similar periodicity along the direction normal to the interface. Such low values of SFEs facilitate nucleation of SFs, which is manifested by long SFs of high linear density. Similarly, low interfacial energies of the $AgSbTe_2/Sb_2Te_3$ system are found to be the reason for high density of $Sb_2Te_3$-precipitates in the AST-matrix, as well [36,37,56–61].

### 4.1. Relation between the planar faults densities and phonon scattering

The lattice thermal conductivity of $Ag_{16.7}Sb_{30}Te_{53.3}$ is very low (0.6–0.7 W $m^{-1}$ $K^{-1}$) at room temperature, which suggests that the phonon mean free path of high fequency phonons is already fully suppressed by the thermal motion of the atoms [12]. Thus, additional phonon scattering processes focusing on low frequency phonons must be introduced beyond phonon-phonon processes when aiming at increasing the figure of merit of this material.

Phonons in solids are scattered by various types of defects, including the planar defects found in this study, which may be effective for scattering of phonons over a wide frequency range [38,62,63]. Small angle grain boundaries are consisting of dislocation arrays. Their high eigen-distortions and associated strain fields should lead to dislocation scattering (and softening) of phonons, and are thus thought to lead to high TE performance in e.g. lead chalcogenides [33,64]. Impurity atoms or vacancies lead to point defect scattering with a scattering rate $\tau^{-1}$ approximately proportional to $\omega^4$ where ω is the phonon angular frequency in the Debye-Callaway model [46]. The linear array of these point defects, which can be used as an approximate model to describe the inner core of a dislocation line, scatter phonons at a factor proportional to $\omega^3$. Similarly, an array of planar defects, as observed in terms of the small angle grain boundaries constituting the mosaic structure revealed in this study, can scatter phonons with a scattering rate proportional to $\omega^2$ due to the dimensionality of the underlying defects [65]. Klemens [66] estimates the scattering rate for SFs, which can be used for the planar faults studied here as:

$$\tau_{SF}^{-1} = \frac{a}{18}\gamma^2\omega^2\ \frac{1}{G_3 v}\cdot\frac{4}{3} \qquad \text{Equation 3}$$

Where $\tau_{SF}$ is the relaxation time for phonon scattering at SFs, γ is the Grüneisen parameter, $v$ is the average sound velocity, and $a$ is the average atomic radius estimated from $a = \sqrt[3]{\overline{V}}$, with $\overline{V}$ being the average atomic volume. The parameter $G_3$ gives the number of atomic layers between two adjacent SFs and can be related to the lattice parameter $a_0$ and SF density $N_{SF}$ [66]:

$$G_3 = \frac{1}{N_{SF}}\cdot\frac{\sqrt{3}}{a_0} \qquad \text{Equation 4}$$

Accordingly, the scattering rate can be written as:

$$\tau_{SF}^{-1} = \frac{2}{27\sqrt{3}}\frac{a}{v}\gamma^2\omega^2 N_{PF} \qquad \text{Equation 5}$$

Here we replaced the stacking fault density by the density of planar faults $N_{PF}$. In order to estimate the possible importance of phonon scattering from planar faults we compare it with the phonon-phonon scattering discussed by Klemens. Phonon-phonon scattering will be dominant above the Debye temperature (138 K for $AgSbTe_2$) [11], and can occur via Umklapp processes and normal processes. These can be expressed as follow [33]:

$$\tau_U^{-1} = \frac{2k_B}{(6\pi^2)^{\frac{1}{3}}}\frac{a\gamma^2\omega^2 T}{\overline{M}v^3} \qquad \text{Equation 6}$$

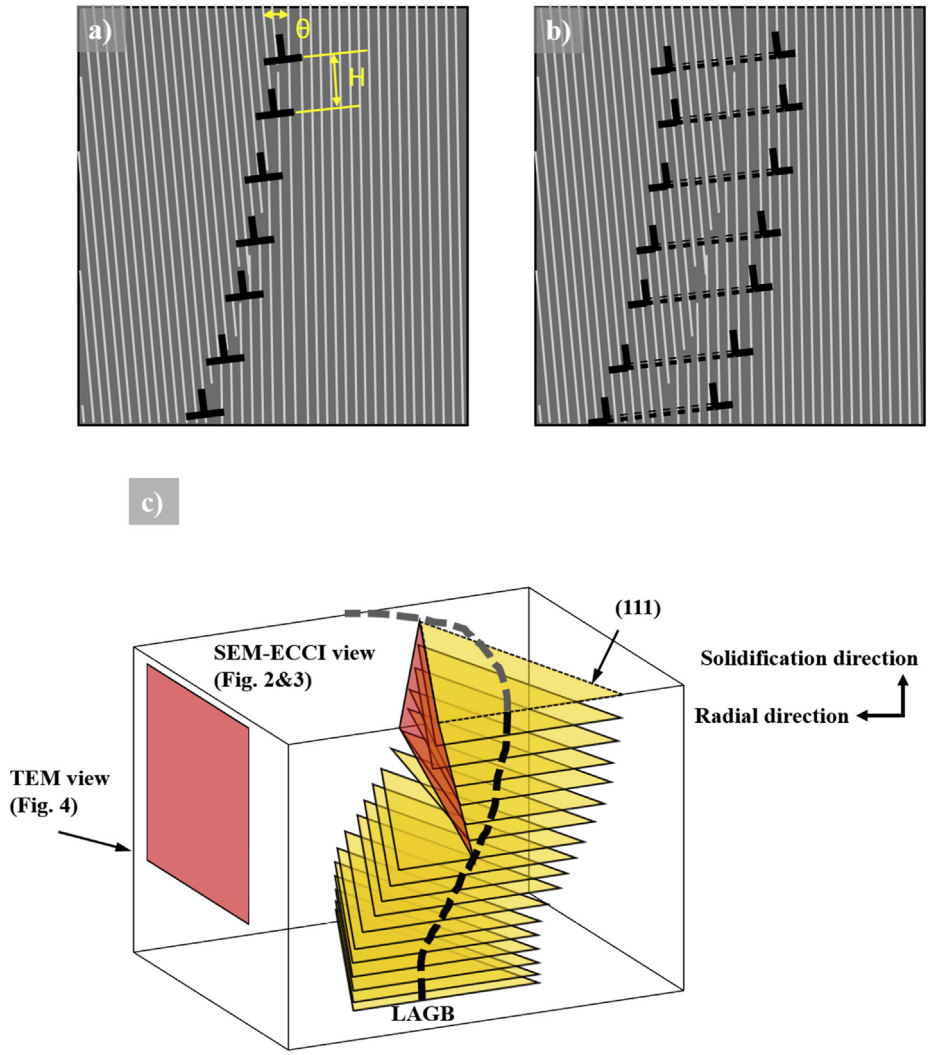


**Fig. 7.** Schematic drawing of a low angle grain boundary formed by (a) perfect dislocations and (b) set of extended planar faults as observed in the current work. (c) Sketch of the arrangement of planar faults lying on (111) planes which are 8° inclined relative to the surface and their observation by SEM-ECCI and TEM cross section.

To calculate the density of planar faults needed to make their scattering as important as the phonon-phonon scattering, we assume $\tau_{SF}^{-1} = \tau_U^{-1}$ and then calculate $N_{PF}$ from equation (5) and equation (6). This operation can be simply implemented for this case, since both expressions depend on ω, although different approaches were previously employed [67]. The necessary $N_{PF}$ can be then estimated to be at (T = 298 K):

$$N_{PF} = 4.5 \cdot 10^5 \cdot 298 = 1.3 \cdot 10^8 m^{-1}$$

All the parameters for the $Ag_{16.7}Sb_{30}Te_{53.3}$ mosaic crystal used for the Debye-Callaway calculation are listed in Table 1 below:

In our material, we determined a planar fault density of $N_{PF} = 1.6 \cdot 10^8\ m^{-1}$ at the LAGB, which is similar to the estimated minimum value of $N_{PF} = 1.3 \cdot 10^8\ m^{-1}$ required to have a notable impact on the thermal conductivity. On the other hand, the planar fault density inside the grain was found to be much lower $N_{PF} = 1.5 \cdot 10^6\ m^{-1}$. It is noteworthy that the LAGBs in this study are primarily parallel to the solidification direction, as discussed at the beginning of the section. Such microstructure is expected to scatter more phonons travelling in a radial direction, thereby deterring the heat flow in the radial direction more efficiently. A polycrystalline microstructure would make such effect more isotropic. In order to make phonon scattering by planar faults more significant, the material needs more volume of LAGBs with a high density of planar faults. For example, as reported by Hong et al. [38], $AgSbTe_{1.85}Se_{0.15}$ with a very fine polycrystalline grain size of ~2 μm and a high number of planar faults has a lattice thermal conductivity of <0.4 $W\,m^{-1}\,K^{-1}$ at room temperature.

**Table 1**
Parameter used in the Debye-Callaway model.

| Parameters | Description | Values |
|---|---|---|
| $\overline{V}$ | Average atomic volume | 22.2 $Å^3$ |
| $\overline{M}$ | Average atomic mass | $2.035 \times 10^{-25}$ kg |
| $v$ | Average sound velocity | 1727 m/s [37,57] |
| $a_0$ | Lattice parameter | 6.2 Å |

## 5. Conclusions

The present results provide insight concerning the statistics and types of the planar faults formed at the grain boundaries of the $Ag_{16.7}Sb_{30}Te_{53.3}$ - δ phase mosaic structure. The sample studied in this work was found to have a different density and distribution of

planar faults at the LAGB and inside the grains. More generally, we demonstrated how ECCI-TEM correlative studies serve the microstructure investigation of $AgSbTe_2$-TE alloys, in particular imaging and calculating the density of planar faults at and away from the grain boundaries. The density of defects calculated from ECCI imaging is similar to the density obtained from TEM analysis. It is important to image these planar faults in a larger scale with the help of ECCI to obtain good statistics on their location and distribution. Processing the relation between the microstructures and TE properties enables to relate the density of planar faults to their effect on the lattice thermal conductivity in an $Ag_{16.7}Sb_{30}Te_{53.3}$ cubic structure through the use of the Debye-Callaway model.

The successful utilization of the correlative approach demonstrated here by selecting different regions containing lattice imperfections in a bulk sample and retrieving their crystallographic features by electron microscopy techniques in a statistically reliable fashion aids future design of microstructure features that are important for enhancing the figure of merit of TE materials. The correlative use of different microstructure probing methods such as ECCI and TEM has proven instrumental for obtaining better understanding of the nature and crystallographic character of the substructure features observed in the material.

## Acknowledgements

This work was supported by a scholarship from the International Max Planck Research School for Interface Controlled Materials for Energy Conversion IMPRS-SurMat. Gerald Jeffrey Snyder acknowledges support from the NIST Center for Hierarchical Materials Design (CHiMaD) contract number 70NANB19H005. Yaron Amouyal acknowledges partial support from the Israel Science Foundation (ISF), Grant No. 1997/18.

## References

[1] Y.H. Ko, M.W. Oh, J.K. Lee, S.D. Park, K.J. Kim, Y.S. Choi, Structural studies of $AgSbTe_2$ under pressure: experimental and theoretical analyses, Curr. Appl. Phys. 14 (11) (2014) 1538–1542.
[2] J. Ma, O. Delaire, A.F. May, C.E. Carlton, M.A. McGuire, L.H. VanBebber, D.L. Abernathy, G. Ehlers, T. Hong, A. Huq, W. Tian, V.M. Keppens, Y. Shao-Horn, B.C. Sales, Glass-like phonon scattering from a spontaneous nanostructure in $AgSbTe_2$, Nat. Nanotechnol. 8 (6) (2013) 445–451.
[3] D.L. Medlin, G.J. Snyder, Atomic-scale interfacial structure in rock salt and tetradymite chalcogenide thermoelectric materials, Jom 65 (3) (2013) 390–400.
[4] B.K. Min, B.S. Kim, I.H. Kim, J.K. Lee, M.H. Kim, M.W. Oh, S.D. Park, H.W. Lee, Electron transport properties of La-doped $AgSbTe_2$ thermoelectric compounds, Electron. Mater. Lett. 7 (3) (2011) 255–260.
[5] R. Mohanraman, R. Sankar, K.M. Boopathi, F.C. Chou, C.W. Chu, C.H. Lee, Y.Y. Chen, Influence of in doping on the thermoelectric properties of an $AgSbTe_2$ compound with enhanced figure of merit, J. Mater. Chem. A 2 (8) (2014) 2839–2844.
[6] R. Mohanraman, R. Sankar, F.C. Chou, C.H. Lee, Y.Y. Chen, Enhanced thermoelectric performance in Bi-doped p-type $AgSbTe_2$ compounds, J. Appl. Phys. 114 (16) (2013) 5.
[7] J.J. Xu, H. Li, B.L. Du, X.F. Tang, Q.J. Zhang, C. Uher, High thermoelectric figure of merit and nanostructuring in bulk $AgSbTe_2$, J. Mater. Chem. 20 (29) (2010) 6138–6143.
[8] M. Zhou, J.F. Li, T. Kita, Nanostructured $AgPb_mSbTe_{m+2}$ system bulk materials with enhanced thermoelectric performance, J. Am. Chem. Soc. 130 (13) (2008) 4527–4532.
[9] Y.Z. Pei, J. Lensch-Falk, E.S. Toberer, D.L. Medlin, G.J. Snyder, High thermoelectric performance in PbTe due to large nanoscale $Ag_2Te$ precipitates and La doping, Adv. Funct. Mater. 21 (2) (2011) 241–249.
[10] G.J. Snyder, E.S. Toberer, Complex thermoelectric materials, Nat. Mater. 7 (2) (2008) 105–114.
[11] V. Jovovic, J.P. Heremans, Doping effects on the thermoelectric properties of $AgSbTe_2$, J. Electron. Mater. 38 (7) (2009) 1504–1509.
[12] D.T. Morelli, V. Jovovic, J.P. Heremans, Intrinsically minimal thermal conductivity in cubic I-V-VI(2) semiconductors, Phys. Rev. Lett. 101 (3) (2008) 4.
[13] H. Wang, J.F. Li, M.M. Zou, T. Sui, Synthesis and transport property of $AgSbTe_2$ as a promising thermoelectric compound, Appl. Phys. Lett. 93 (20) (2008) 3.
[14] K.T. Wojciechowski, M. Schmidt, Structural and thermoelectric properties of $AgSbTe_2$-$AgSbSe_2$ pseudobinary system, Phys. Rev. B 79 (18) (2009) 7.
[15] R.M. Marin, G. Brun, J.C. Tedenac, Phase-Equilibria in the $Sb_2Te_3$-$Ag_2Te$ system, J. Mater. Sci. 20 (2) (1985) 730–735.
[16] S. Geller, J.H. Wernick, Ternary semiconducting compounds with sodium chloride-like structure- $AgSbSe_2$, $AgSbTe_2$, $AgBiS_2$, $AgBiSe_2$, Acta Crystallogr. 12 (1) (1959) 46–54.
[17] A. Castellero, G. Fiore, E. Evenstein, M. Baricco, Y. Amouyal, Effects of rapid solidification on phase formation and microstructure evolution of $AgSbTe_2$-based thermoelectric compounds, J. Nanosci. Nanotechnol. 17 (3) (2017) 1650–1656.
[18] V. Jovovic, J.P. Heremans, Measurements of the energy band gap and valence band structure of $AgSbTe_2$, Phys. Rev. B 77 (24) (2008) 8.
[19] R. Wolfe, J.H. Wernick, S.E. Haszko, Anomalous Hall effect in $AgSbTe_2$, J. Appl. Phys. 31 (11) (1960) 1959–1964.
[20] M. Zhu, O. Cojocaru-Miredin, A.M. Mio, J. Keutgen, M. Kupers, Y. Yu, J.Y. Cho, R. Dronskowski, M. Wuttig, Unique bond breaking in crystalline phase change materials and the quest for metavalent bonding, Adv. Mater. 30 (18) (2018) 9.
[21] F.D. Rosi, E.F. Hockings, N.E. Lindenblad, Semiconducting materials for thermoelctric power generation Rca review 22 (1) (1961) 82–121.
[22] C. Wood, Materials for thermoelectric energy-conversion, Rep. Prog. Phys. 51 (1988) 459–539.
[23] H. Wang, J.F. Li, C.W. Nan, M. Zhou, W.S. Liu, B.P. Zhang, T. Kita, High-performance $Ag_{0.8}Pb_{18+x}SbTe_{20}$ thermoelectric bulk materials fabricated by mechanical alloying and spark plasma sintering, Appl. Phys. Lett. 88 (9) (2006) 3.
[24] B.A. Cook, M.J. Kramer, X. Wei, J.L. Harringa, E.M. Levin, Nature of the cubic to rhombohedral structural transformation in $(AgSbTe2)_{(15)}(GeTe)_{(85)}$ thermoelectric material, J. Appl. Phys. 101 (5) (2007) 6.
[25] T. Schroder, T. Rosenthal, N. Giesbrecht, M. Nentwig, S. Maier, H. Wang, G.J. Snyder, O. Oeckler, Nanostructures in Te/Sb/Ge/Ag (TAGS) thermoelectric materials induced by phase transitions associated with vacancy ordering, Inorg. Chem. 53 (14) (2014) 7722–7729.
[26] S.H. Yang, T.J. Zhu, T. Sun, S.N. Zhang, X.B. Zhao, J. He, Nanostructures in high-performance $(GeTe)_{(x)}(AgSbTe_{(2)})_{(100-x)}$ thermoelectric materials, Nanotechnology 19 (24) (2008) 5.
[27] K.F. Hsu, S. Loo, F. Guo, W. Chen, J.S. Dyck, C. Uher, T. Hogan, E.K. Polychroniadis, M.G. Kanatzidis, Cubic $AgPb_mSbTe_{2+m}$: bulk thermoelectric materials with high figure of merit, Science 303 (5659) (2004) 818–821.
[28] S. Roychowdhury, R. Panigrahi, S. Perumal, K. Biswas, Ultrahigh thermoelectric figure of merit and enhanced mechanical stability of p-type $AgSb_{1-x}Zn_xTe_2$, Acs Energy Lett. 2 (2) (2017) 349–356.
[29] J.D. Sugar, D.L. Medlin, Solid-state precipitation of stable and metastable layered compounds in thermoelectric $AgSbTe_2$, J. Mater. Sci. 46 (6) (2010) 1668–1679.
[30] P.A. Sharma, J.D. Sugar, D.L. Medlin, Influence of nanostructuring and heterogeneous nucleation on the thermoelectric figure of merit in $AgSbTe_2$, J. Appl. Phys. 107 (11) (2010) 9.
[31] M.S. Dresselhaus, G. Chen, M.Y. Tang, R.G. Yang, H. Lee, D.Z. Wang, Z.F. Ren, J.P. Fleurial, P. Gogna, New directions for low-dimensional thermoelectric materials, Adv. Mater. 19 (8) (2007) 1043–1053.
[32] H.-S. Kim, S.D. Kang, Y. Tang, R. Hanus, G. Jeffrey Snyder, Dislocation strain as the mechanism of phonon scattering at grain boundaries, Mater. Horiz. 3 (3) (2016) 234–240.
[33] Z.W. Chen, Z.Z. Jian, W. Li, Y.J. Chang, B.H. Ge, R. Hanus, J. Yang, Y. Chen, M.X. Huang, G.J. Snyder, Y.Z. Pei, Lattice dislocations enhancing thermoelectric PbTe in addition to band convergence, Adv. Mater. 29 (23) (2017) 8.
[34] J. He, S.N. Girard, M.G. Kanatzidis, V.P. Dravid, Microstructure-lattice thermal conductivity correlation in nanostructured $PbTe_{0.7}S_{0.3}$Thermoelectric materials, Adv. Funct. Mater. 20 (5) (2010) 764–772.
[35] C. Dames, Thermal conductivity of nanostructered thermoelectric materials, in: D.M. Rowe (Ed.), CRC Handbook of Thermoelectrics, CRC Press Inc, Boca Raton, 2005 section III 42.
[36] P.A. Sharma, J.D. Sugar, D.L. Medlin, Influence of nanostructuring and heterogeneous nucleation on the thermoelectric figure of merit in $AgSbTe_2$, J. Appl. Phys. 107 (11) (2010).
[37] Y. Amouyal, Reducing lattice thermal conductivity of the thermoelectric compound $AgSbTe_2$ (P4/mmm) by lanthanum substitution: computational and experimental approaches, J. Electron. Mater. 43 (10) (2014) 3772–3779.
[38] M. Hong, Z.G. Chen, L. Yang, Z.M. Liao, Y.C. Zou, Y.H. Chen, S. Matsumura, J. Zou, Achieving $zT > 2$ in p-type $AgSbTe_{2-x}Se_x$ alloys via exploring the extra light valence band and introducing dense stacking faults, Adv. Energy Mater. 8 (9) (2018) 7.
[39] O. Cojocaru-Miredin, L. Abdellaoui, M. Nagli, S. Zhang, Y. Yu, C. Scheu, D. Raabe, M. Wuttig, Y. Amouyal, Role of nanostructuring and microstructuring in silver antimony telluride compounds for thermoelectric applications, ACS Appl. Mater. Interfaces 9 (17) (2017) 14779–14790.
[40] C.G. Darwin, The reflexion of X-rays from imperfect crystals, Philos. Mag. 43 (257) (1922) 800–829.
[41] F. Zwicky, Secondary structure and mosaic structure of crystals, Phys. Rev. 40 (1) (1932) 63–77.
[42] A.O. Er, J. Tang, J. Chen, P.M. Rentzepis, Time-resolved X-ray diffraction studies of laser-induced acoustic wave propagation in bilayer metallic thin crystals, J. Appl. Phys. 116 (9) (2014).
[43] M.W. Geis, Device quality diamond substrates, Diam. Relat. Mat. 1 (5–6) (1992) 684–687.
[44] Y. He, P. Lu, X. Shi, F.F. Xu, T.S. Zhang, G.J. Snyder, C. Uher, L.D. Chen, Ultrahigh thermoelectric performance in mosaic crystals, Adv. Mater. 27 (24) (2015)

3639–3644.
[45] S. Zaefferer, N.N. Elhami, Theory and application of electron channelling contrast imaging under controlled diffraction conditions, Acta Mater. 75 (2014) 20–50.
[46] J. Callaway, H.C. von Baeyer, Effect of point imperfections on lattice thermal conductivity, Phys. Rev. 120 (4) (1960) 1149–1154.
[47] M. Schaffer, B. Schaffer, Q. Ramasse, Sample preparation for atomic-resolution STEM at low voltages by FIB, Ultramicroscopy 114 (2012) 62–71.
[48] R.M. Martin, Electronic Structure: Basic Theory and Practical Methods, Cambridge universtiy press, Cambridge, UK, 2004.
[49] G.M.N. Argaman, Density functional theory - an introduction, Am. J. Phys. 68 (69) (1998) 69–79.
[50] Y. Mishin, M. Asta, J. Li, Atomistic modeling of interfaces and their impact on microstructure and properties, Acta Mater. 58 (4) (2010) 1117–1151.
[51] G. Kresse, Efficient iterative schemes for ab initio total-energy calculations using a plane-wave basis set, Phys. Rev. B 54 (16) (1996) 11169–11186.
[52] G. Kresse, From ultrasoft pseudopotentials to the projector augmented-wave method, Phys. Rev. B 59 (1999) 1758–1775.
[53] A.R.J.P. Perdew, G.I. Csonka, O. a. Vydrov, G.E. Scuseria, L. a. Constantin, X. Zhou, K. Burke, Generalized gradient approximation for solids and their surfaces, Phys. Rev. Lett. 100 (136406) (2007) 1–4.
[54] Y.N. Picard, M. Liu, J. Lammatao, R. Kamaladasa, M. De Graef, Theory of dynamical electron channeling contrast images of near-surface crystal defects, Ultramicroscopy 146 (2014) 71–78.
[55] Y. Amouyal, Silver-Antimony-Telluride: from First-Principles Calculations to Thermoelectric Applications, Intech Europe, Rijeka, 2016.
[56] J.D. Sugar, D.L. Medlin, Precipitation of Ag2Te in the thermoelectric material $AgSbTe_2$, J. Alloy. Comp. 478 (1–2) (2009) 75–82.
[57] Y. Amouyal, On the role of lanthanum substitution defects in reducing lattice thermal conductivity of the $AgSbTe_2$ (P4/mmm) thermoelectric compound for energy conversion applications, Comput. Mater. Sci. 78 (2013) 98–103.
[58] D.L. Medlin, J.D. Sugar, Interfacial defect structure at $Sb_2Te_3$ precipitates in the thermoelectric compound $AgSbTe_2$, Scr. Mater. 62 (6) (2010) 379–382.
[59] S.N. Zhang, T.J. Zhu, S.H. Yang, C. Yu, X.B. Zhao, Phase compositions, nanoscale microstructures and thermoelectric properties in $Ag_{2-y}Sb_yTe_{1+y}$ alloys with precipitated $Sb_2Te_3$ plates, Acta Mater. 58 (12) (2010) 4160–4169.
[60] B.G. Ayral-Marin RM, M. Maurin, J.C. Tedenac, Contribution to the study of $AgSbTe_2$, Euro. J. Solid State Chem. 27 (1990) 747–757.
[61] H.-J. Wu, S.-W. Chen, Phase equilibria of Ag–Sb–Te thermoelectric materials, Acta Mater. 59 (16) (2011) 6463–6472.
[62] B.K. Singh, V.J. Menon, K.C. Sood, Phonon conductivity of plastically deformed crystals: role of stacking faults and dislocations, Phys. Rev. B 74 (18) (2006) 6.
[63] M. Hong, Z.G. Chen, L. Yang, Y.C. Zou, M.S. Dargusch, H. Wang, J. Zou, Realizing zT of 2.3 in $Ge_{1-x-y}Sb_xIn_yTe$ via reducing the phase-transition temperature and introducing resonant energy doping, Adv. Mater. 30 (11) (2018) 8.
[64] R. Hanus, M.T. Agne, A.J.E. Rettie, Z. Chen, G. Tan, D.Y. Chung, M.G. Kanatzidis, Y. Pei, P.W. Voorhees, G.J. Snyder, Lattice softening significantly reduces thermal conductivity and leads to high thermoelectric efficiency, Adv. Mater. 31 (21) (2019), e1900108.
[65] R. Hanus, A. Garg, G.J. Snyder, Phonon diffraction and dimensionality cross-over in phonon-interface scattering, Commun. Phys. 1 (2018) 11.
[66] P. Klemens, Some scattering problems in conduction theory, Can. J. Phys. 35 (4) (1957) 441–450.
[67] Y. Amouyal, Silver-antimony-telluride: from first-principles calculations to thermoelectric applications, in: Thermoelectrics for Power Generation - A Look at Trends in the Technology, 2016.